Coulomb expansion of a cold non-neutral rubidium plasma

Michael A. Viray ⬤, Stephanie A. Miller,[*] and Georg Raithel

Department of Physics, University of Michigan, Ann Arbor, Michigan 48109, USA

We study the expansion of a cold, non-neutral ion plasma into the vacuum. The plasma is initialized by photoionization of cold rubidium atoms in a magneto-optical trap by an ultraviolet laser pulse. We employ time-delayed plasma extraction and imaging onto a position- and time-sensitive microchannel plate detector to analyze the plasma. We report on the formation and persistence of plasma shock shells, pair correlations in the plasma, and external-field-induced plasma focusing effects. We also develop trajectory and fluid descriptions to model the data and to gain further insight. The simulations verify the formation of shock shells and correlations, and allow us to model time- and position-dependent density, temperature, and Coulomb coupling parameter, $\Gamma(\mathbf{r}, t)$. The analysis also shows that the experimental plasma is strongly coupled and elucidates its expansion dynamics.

I. INTRODUCTION

The development of atom trapping and cooling processes [1] has made it possible for researchers to photoexcite cold plasmas in the laboratory [2–5]. This enables models that scale to hard-to-access plasmas that occur, for instance, in astrophysical environments (insides of stars and gas planets) [6], magnetic-confinement fusion [7,8], and inertial-confinement fusion [9,10]. Recent work in cold plasma physics has explored plasma laser cooling [11], pair correlations [12–15], dual-species ion collisions [16,17], Rydberg atom-plasma interactions [18], plasma field-sensing applications [19–21], and quenched randomness and localization [22].

One area of interest in laboratory plasma physics is the expansion of plasma into vacuum [23–25], a topic that has been of interest, for instance, because of its parallels to astrophysical systems [26,27]. The central topic of this paper is non-neutral-plasma expansion, also known as Coulomb explosion [19,28,29]. Expanding non-neutral plasmas can exhibit several interesting phenomena such as vortices [30] and Bernstein modes [31]. The phenomena of greatest interest in our paper are shock shells and strong coupling. Shock shells form in Coulomb explosions if, initially, the outer layer of ions is less dense than the center [32,33]. If so, intermediate layers of the plasma tend to catch up with peripheral layers, and form a higher-density shock shell. Shock fronts form in both spherically symmetric and cylindrically symmetric plasmas [32]. They can form in a wide variety of non-neutral plasmas, including relativistic electron clouds [34]. Rapidly expanding plasmas also are intriguing thermodynamic systems [25]. As the plasma expands, the temperature changes globally in time due to disorder-induced heating and adiabatic cooling [35], and locally in space across the shock shells [33].

In the present work, we perform measurements on the Coulomb expansion of initially cold, laser-excited microplasmas prepared from a rubidium magneto-optic trap (MOT). The plasmas contain a few-hundred ions and have initial diameters of tens of microns. Central to our work are ion imaging techniques using electric fields, and single-ion-counting microchannel plate detectors. These methods have been used before on Rydberg atoms in order to observe blockade radii [36], van der Waals interactions [37], ionization spectra [38,39], and tunnel ionization rates [40]. Here, we use ion imaging to observe the free expansion, shock shells, and correlations in microplasmas as a function of expansion time.

In the computational component of our work, we model the plasma expansion using a molecular dynamics model and a fluid model. The molecular dynamics simulation accurately models micro- and macroscopic aspects of the plasma, including its particle correlations and shock fronts. This model yields time-dependent maps of the ion volume density n_V, the ion temperature T, and other variables that shed light on the transient thermodynamic behavior of the system, including the presence of shock shells and strong coupling. The fluid model provides a fast means to qualitatively model and interpret the shock fronts in the limit of vanishing microscopic effects.

The temperature and density distributions found in the computational work also lead into a discussion of the plasma's Coulomb coupling strength Γ, defined as

$$\Gamma = \frac{q^2/(4\pi\varepsilon_0 r_{WS})}{k_B T}, \tag{1}$$

with the ion charge q, the vacuum permittivity ε_0, the Boltzmann constant k_B, and the Wigner-Seitz radius $r_{WS} = \sqrt[3]{3/(4\pi n_V)}$. A plasma is considered strongly coupled when $\Gamma \gtrsim 1$. While Eq. (1) is often employed in uniform plasmas in thermal equilibrium, it can also be used to describe plasmas that evolve in time or that are nonuniform, such as our expanding rubidium-ion plasmas, which are sufficiently

---

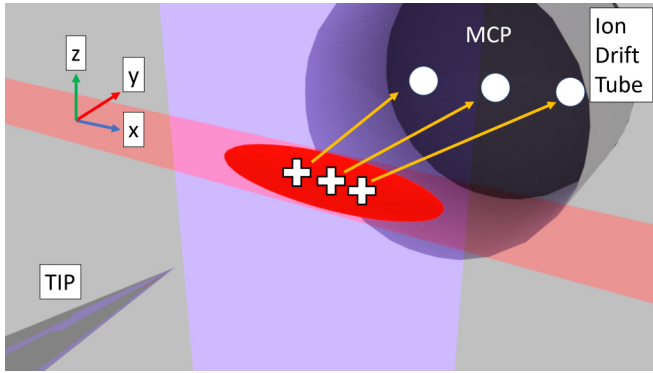[*]Present address: Terumo Heart, Inc., Ann Arbor, MI 48103, USA.

FIG. 1. Rendering of experimental setup and process of plasma formation and imaging (not to scale). The positively charged rubidium ions are accelerated by the TIP electric field through the ion drift tube to the MCP, where they produce blips of a few-hundred ns decay time that are imaged with a camera.

close to local equilibrium. In this case, Γ becomes both time and position dependent, based on local densities $n_V(\mathbf{r}, t)$ and temperatures $T(\mathbf{r}, t)$ defined on suitable spatial regions. The determination of time- and position-dependent n_V, T, and Γ is less straightforward than in steady-state systems; yet we use these parameters because they lend themselves to an efficient description of our expanding microplasmas based on a small set of thermodynamic variables.

II. EXPERIMENTAL SETUP

We employ a ^{87}Rb MOT from which the plasma is formed. Details of the atomic-physics package are described in the Appendix. In each experimental cycle, a plasma containing up to several hundreds of ions is formed from the MOT by resonant two-photon photoionization with a 10 ns laser pulse. The laser-beam shapes define the initial plasma shape, which is a cylinder with several 100 μm in length and several tens of μm in diameter. The liberated photoionization electrons have a kinetic energy of 0.9 eV, which is sufficient for the electrons to escape the plasma cloud. The temperature of the atoms before photoionization ($\sim$100 μK) as well as any atom heating due to radiation pressure from the photoionization lasers are not important. The photoionization is accompanied by an ion recoil energy of 5.8 μeV, equivalent to an initial ion temperature in the plasma of 44 mK.

The MOT chamber contains a needle-shaped, beryllium-copper tip imaging probe (TIP), which is positioned $\sim$2 mm away from the photoionization region. Figure 1 shows the orientation of the plasma, TIP, and other experimental components. After the plasma has been formed, it undergoes free expansion for a variable wait time τ. After the wait time, a high-voltage square pulse with a 90% rise time of 76 ns is applied to the TIP, producing a divergent strong electric field. The ions are accelerated by this electric field towards a microchannel plate (MCP) located about 25 cm away. Upon impact on the MCP, the ions produce bright spots on a phosphor screen, which provide information on the plasma ion positions at the time of extraction. The MCP detection efficiency is 30–50%, according to the manufacturer's specifications. A CCD camera takes a picture of the phosphor

screen for each experimental cycle. The single-ion-resolving images represent the plasma ion distributions after the free-expansion time τ, projected onto a plane transverse to the extraction direction. The magnification factor of the imaging setup can be varied by adjusting the distance between the TIP and the excitation region and can be calibrated by translating the excitation region by known distances. The spatial structure of the plasma transverse to the MCP plane (i.e., along the extraction direction) is analyzed by measuring its time-of-flight distribution to the MCP using a multichannel scaler (SRS Model SR430).

III. COMPUTER MODELING

We use two approaches to model our system. In the molecular dynamics simulations, we calculate trajectories of up to 1000 ions, accounting for all external and interparticle Coulomb forces. A numerically generated map of the electrostatic potential along the ion-imaging path between the TIP and the MCP is implemented to model the ion imaging. While this approach is computationally expensive due to the need to account for binary forces, it has the following strengths: (1) it is exact, limited in particle number only by computing power; (2) the ion-extraction timing, the analysis of the ion images on the MCP, the ion time-of-flight data, and the pair-correlation functions closely follow the experimental procedure; and (3) valuable insights on macroscopic plasma parameters such as expansion velocity, density, temperature, coupling parameter, etc. can be obtained on a grid of spatial domains as a function of time. The trajectory simulation is exact because it accounts for microscopic and macroscopic electric fields (here, there are no significant magnetic fields), initial ion velocities and their angular distribution, initial spatial ion distributions, and Coulomb collisions during free expansion, ion extraction, and imaging. The trajectory simulations are well suited to model correlations and strong-coupling effects, in addition to modeling the overall expansion and imaging dynamics.

In the second approach, the plasma is modeled as a collisionless medium (fluid) with a fixed charge-to-mass ratio that evolves under the influence of the macroscopic plasma electric field. In this collision-free, zero-temperature approach, the plasma is numerically treated as a discrete set of thin, interpenetrable cylindrical or spherical shells. The initial photon-recoil-induced ion motion is ignored. The initial charges on the shells are given by the initial shell radii, shell thicknesses, and the initial charge distribution, which depends on ion excitation parameters and atom densities (chosen similar to those used in the experiment). The discrete radii of the shells are then propagated using Newton's equations. Gauss's law is employed to track the macroscopic electric field at the locations of the shells. The dynamical variables in this model are the shell radii and velocities, and the plasma electric field. This model ignores the effects of the microscopic fields and collisions; therefore, it cannot be used to model particle correlations. Also, in its present form, the model does not allow for the inclusion of extraction and imaging electric fields that do not share the symmetry of the charge distribution. Nevertheless, the fluid model is numerically inexpensive and suitable for the generation of qualitative plasma density maps versus time during the free-expansion time of the plasma. In the
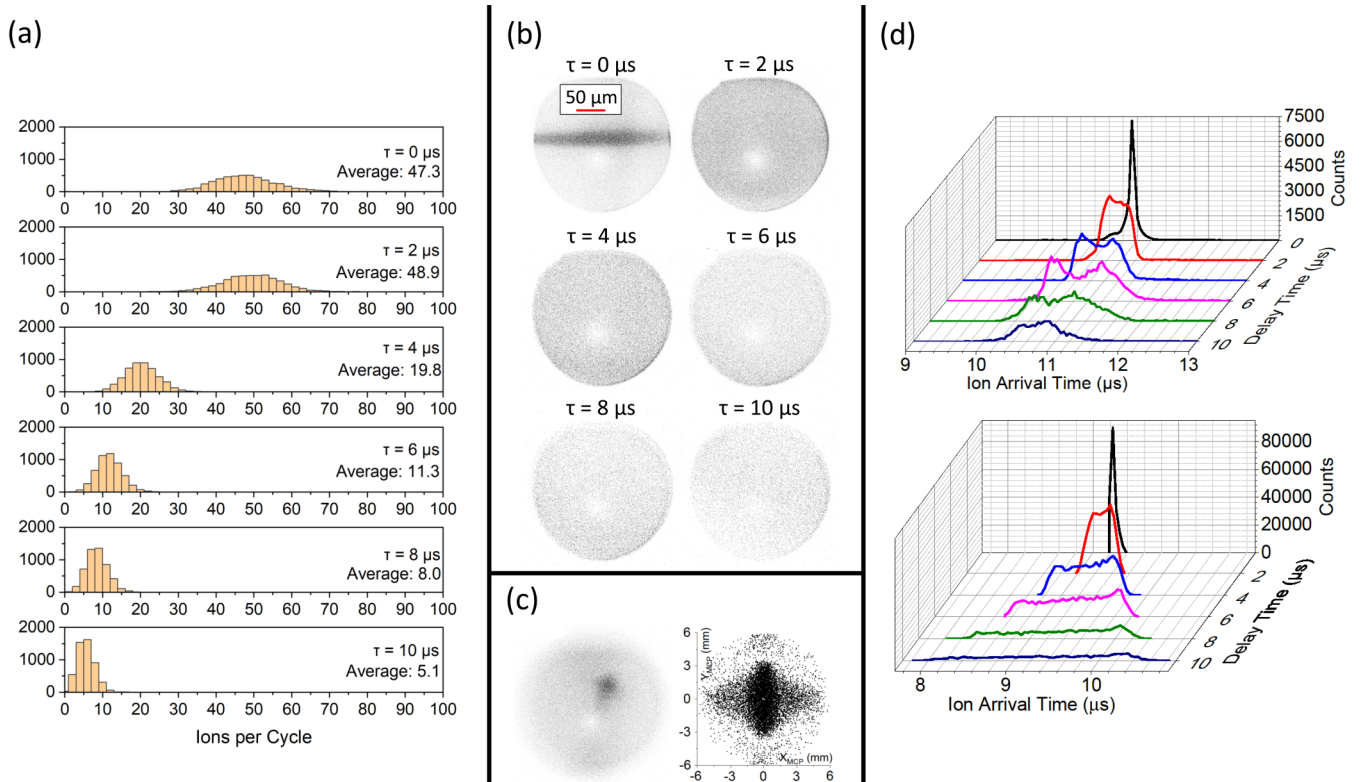
FIG. 2. (a) Histograms of ion counts per cycle for the indicated expansion times τ. (b) Averaged pictures of the plasma images on the MCP plane for the indicated expansion times. The distance scale in the upper-left image corresponds to the distance in the object plane. The light spot is an area of reduced ion detection rate; its origin is under investigation. (c) Experimental (left) and computational (right) MCP images of plasma at $\tau = 10\ \mu$s in the presence of a quadrupole electric field. Instead of expanding outwards and leaving the field of view, the ions are refocused by the electric field and accumulate at a plasma focus, which maps onto a localized region on the MCP with well-above-average count density. (d) Experimental (top) and computational (bottom) distributions of ion MCP arrival times (horizontal axis) for different plasma expansion times (tilted axis). To enhance visibility, the count axes for the experimental data are magnified by factors of 1, 2, 4, 8, 8, and 8, in ascending order of expansion times. Likewise, the count axes for the computational data are magnified by factors of 1, 8, 32, 64, 64, and 64.

fluid model, shock fronts appear as singularities of the plasma density. Comparison between the fluid and the molecular dynamics models then allows us to distinguish macroscopic from microscopic field effects. A detailed analysis based on these models is given in Sec. V.

IV. EXPERIMENTAL RESULTS

A. Expansion dynamics

In our experimental work, plasmas are excited from Rb atom clouds in a MOT, as described in Sec. II. The MOT contains 3.8×10^7 atoms at a density of 4.1×10^{11} atoms/cm^3, as determined by shadow imaging. The spatial profile of the initial ion clouds is given by the geometry described in Sec. II and the Appendix. The actual number of ions within the fixed field of view is 100 to 150, based on ion count and MCP detection efficiency. The initial central ion density is $n \approx 10^{10}$ cm^{-3}, as determined from ion number and excitation geometry. We observe this plasma for $\tau = 0$, 2, 4, 6, 8, and 10 μs of free-expansion time. Ion-density images, time-of-flight data, and pair-correlation functions are averaged over 5000 experimental realizations. The linear image magnification factor for this dataset is 54 times, with a diameter of the field of view on the MCP of 12 mm.

The density and initial ion kinetic energy from photoionization recoil indicate an initial Debye length of $\lambda_D \sim 1\ \mu$m, more than a factor of ten less than the short-axes initial diameter of the ion cloud, and an initial Coulomb coupling parameter of $\Gamma \approx 50$ [following Eq. (1)]. Shortly after plasma generation, the temperature and coupling parameter undergo a rapid increase and decrease, respectively, caused by disorder-induced heating. Several-hundred nanoseconds into the Coulomb expansion, adiabatic cooling associated with the free Coulomb expansion leads to a recovery of these parameters. Our molecular dynamics simulations provide considerable insight into these dynamics, as discussed in detail in Sec. V.

Figures 2(a) and 2(b) show the experimentally observed ion-count statistics and averaged images of plasma expansion. Starting from its initial cylindrical shape, seen at $\tau = 0\ \mu$s, the plasma ions rapidly accelerate outward, leading to overall plasma expansion. At $\tau = 2\ \mu$s, the plasma approximately fills the field of view along its initially short axis, with the average ion count still remaining approximately constant. For longer expansion times, the ions leave the field of view, and the average ion count monotonically decreases. Over the course of 10 μs of free-expansion time, the ion count decreases to about 10% of the initial value.

Figure 2(d) shows the experimental and simulated MCP arrival-time distributions of the plasma ions for each expansion time τ. The arrival-time traces have been aligned on the time axis so that the firing of the TIP imaging voltage pulse is at $t = 0$ (equivalent to the end of the expansion time τ). As τ increases, the ion arrival-time distribution develops a leading and a lagging peak, signaling the formation of shock shells. As the plasma expands radially, a fraction of ions move toward the TIP, while another fraction of ions moves in the opposite direction toward the MCP. When the TIP electric field is engaged, the ions closer to the TIP experience a stronger electric field than ions that are farther away. Hence, the longitudinal position distribution of the ions maps onto a time-of-flight distribution in which shorter times of flight correspond to ions closer to the TIP at the onset of the TIP imaging voltage pulse. The peaks in the time-of-flight distribution correspond to shells of enhanced plasma density, or shock fronts. In our data in Fig. 2(d), the shock fronts begin to form at $\tau = 4$ μs and are most prominent at $\tau = 6$ μs. While this scenario is well supported by the simulations that underlie the numerical data in Fig. 2, it is noted that experimental and simulated arrival-time distributions begin to differ from each other at about $\tau = 6$ μs and onward. These differences are attributed to details of the ion-imaging electric field in the chamber that come to bear once the plasma has significantly expanded off-axis. These fields may, in part, be the result of unknown higher-order multipoles of the TIP electric field, geometrical imperfections, and stray potentials.

B. Plasma focus

Additional experimental evidence for the importance of higher-order multipole electric fields is found in that it is not sufficient to zero the leading (dipolar) background electric field at the location of the initial plasma cloud. We also need to zero the linear (quadrupolar) components of the field in order to achieve undistorted plasmas at long expansion times τ. This is possible in our setup because it has nine electric-field compensation electrodes. Incomplete field zeroing results in a quadrupole field with a field zero inside the initial plasma cloud that typically causes the expanding plasma to refocus along certain directions of space, while defocusing along other (orthogonal) directions. Figure 2(c) shows experimental and computational MCP images of a plasma at $\tau = 10$ μs in the presence of a quadrupole field that focuses the ions in the xz plane and defocuses along the y direction (coordinates defined in Fig. 1). In this case, the plasma focus generated by the quadrupole field manifests in a localized, kite-shaped region on the MCP of enhanced ion-count density. The kite shape arises from an astigmatism caused by the azimuthal dependence of the initial plasma cloud around the y direction (see Fig. 1). In the present work, we have thoroughly field zeroed the dipolar and quadrupolar field components to avoid this plasma focus effect. Nevertheless, remaining higher-order multipolar and other field perturbations are suspected as the main cause of the deviations between the experimental and simulated data at long expansion times.
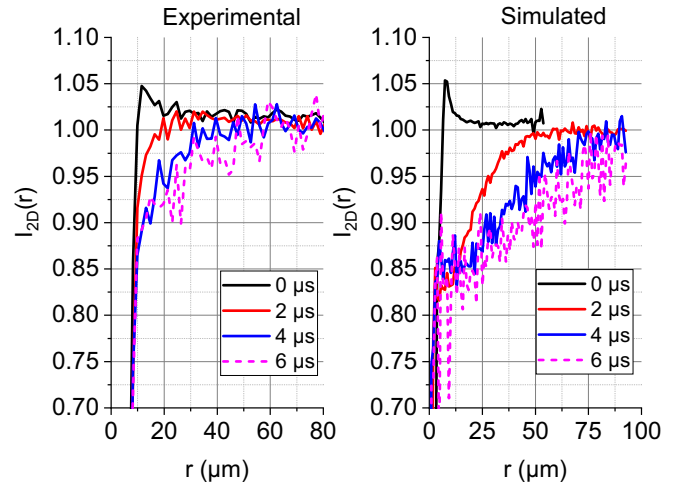

FIG. 3. Projected, two-dimensional ion pair correlations $I_{2D}(r)$ for the indicated expansion times, measured vs the radial coordinate in the xz object plane. The left panel is for experimental data and the right one for simulated data. Pair correlations for $\tau > 6$ μs are not shown because they are too noisy, as a result of the diminishing ion number in the images. The steep drop in the data at distances $\lesssim 8$ μm is an experimental artifact caused by the finite blip size of the ion counts on the MCP.

C. Pair-correlation function

As indicated above, the plasma may, in addition to shock fronts, also exhibit strong coupling, which should lead to structures in the pair-correlation function $I(r)$ caused by Coulomb repulsion. From the experimental data, we calculate pair correlations $I_{2D}(r)$ between ion counts in the images projected onto the two-dimensional (2D) MCP plane. This is done for each expansion time τ. We first process the raw images with a peak finder algorithm, then obtain the pair correlation of the peaks, and then normalize the repetition-averaged pair correlation such that a value of one corresponds to an absence of correlations. Since the processing is performed on impact positions in the image plane (the MCP surface), which the ions reach ~ 10 μs after application of the high-voltage ion-extraction pulse, the $I_{2D}(r)$ are magnified, time-propagated representations of correlations that exist at the time instant of ion extraction. In the data displayed, projected distances on the MCP image plane are divided by magnification (here, 54) to obtain projected distances r in the object plane. For more details on this method, see [36,37].

In Fig. 3, we show the functions $I_{2D}(r)$ in the object plane for the indicated values of τ. The data are averages over 5000 repetitions for each expansion time. The $I_{2D}(r)$ reveal anticorrelation, $I_{2D}(r) < 1$, out to a distance that increases with τ, reaching ≈ 50 μm at $\tau = 6$ μs. At $\tau \gtrsim 0$ μs, there is a region of enhanced correlation, $I_{2D}(r) > 1$, at $r \sim 10$ μm. The correlations are due to the microfields in the plasma, which cause disorder-induced heating [41] and subsequent buildup of strong correlations.

It is noted that the values of $I_{2D}(r)$ for small r do not drop below ≈ 0.9. This is due to the fact that the measured pair correlations represent three-dimensional particle configurations projected into the xz plane. Since the expanding

plasma extends multiple correlation distances along the line of sight (the y direction), the true 3D correlation function becomes washed out in the course of projecting it onto a 2D image plane. In the 2D image, initially distant, uncorrelated ions can have projections that accidentally appear close to each other, thereby mimicking an ion pair at a very short distance. Nevertheless, the experimental and simulated data qualitatively agree in the degree of residual anticorrelation at short distances, $I_{2D}(r \sim 10 \ \mu m) \approx 0.9$, in the experiment vs 0.85 in the simulation. Also, there is a significant degree of positive correlation, $I_{2D}(r \sim 10 \ \mu m) - 1 \approx 0.05$, at near-zero expansion time τ, both in the experiment and simulation. Further, the shapes of the functions $I_{2D}(r)$ and the range in expansion time τ over which the domain of anticorrelation expands qualitatively agrees between the experiment and simulation. It is observed that the spatial extent of anticorrelation in the experiment is less than that in the simulation (see Fig. 3). We attribute this difference to the effects of higher-order multipolar fields and other field perturbations that act along the 25-cm-long ion-extraction trajectories.

As discussed in the following section, ion correlations are more evident in the three-dimensional (3D) pair-correlation function, $I_{3D}(r)$, than in $I_{2D}(r)$. While the experiment would require a technology change to track $I_{3D}(r)$, the molecular dynamics simulation discussed next allow this without additional effort.

V. NUMERICAL STUDY OF ION-PLASMA EXPANSION

A. Details of molecular dynamics model

The experimental and computational results already presented provide evidence for ion correlations that may indicate strong coupling, as well as for shock fronts. In the following, we study the expanding plasma by tracking the spatiotemporal evolution of a set of macroscopic parameters. Most of this computational work is done with a molecular dynamics simulation that accounts for all Coulomb and external forces. Here we describe the simulation method in some detail. In order to highlight the essential physics, we mostly model the expansion of spherically symmetric plasmas into field-free space. The molecular dynamics simulation is quite flexible, though; it has been employed, for instance, to generate Figs. 2(c), 2(d) (lower panel), and Fig. 3 (right panel) to model our experiment in considerable detail.

The particle system is large enough to describe its dynamics via time- and position-dependent macroscopic parameters in subvolumes of the plasma that are close to a local equilibrium. To arrive at a suitable size and simple shape of the subvolumes in the expanding plasma, in this section we restrict our study to a spherically symmetric system without external forces, so as to maintain macroscopic spherical symmetry. This allows us to break up the plasma into spherical partitions (shells) with a certain thickness, within which we find the local thermodynamic parameters versus time.

As a guide for what constitutes a suitable shell number, we note that the correlation length evident from the above-discussed correlation functions is of the order of 10% of the typical system diameter. Based on this, the plasma is divided into ten partitions: the core and nine shells. Each

partition contains one-tenth of all plasma particles. Further, for computation of the temperature and Coulomb coupling parameter, we dynamically adjust the shell radii and thicknesses so that there is always 10% of the ions in each of the 10 shells. For instance, for a plasma of 150 particles, the outer radius of the innermost shell, $i = 1$, is the average of the radial coordinates of the 15th and the 16th particle, after sorting the particles in ascending order of their radii, and so on. Radial coordinates are measured relative to the symmetry center of the plasma. The dynamic variables in each simulation include the inner and outer radii of the shells, $r_{\mathrm{in},i}(t)$ and $r_{\mathrm{out},i}(t)$, with shell index $i = 1, 2, \ldots, 10$, and the ion-averaged shell radii $r_i(t)$ and velocities $v_i(t)$. As the plasma expands, all shell radii expand. Ions are allowed to switch between adjacent shells so as to maintain a fixed number of ions in the shells.

From $r_{\mathrm{in},i}(t)$ and $r_{\mathrm{out},i}(t)$, we directly get the time-dependent shell volumes. The ion densities $n_{V,i}(t)$ of the shells are then given by the fixed ion numbers in the shells divided by the shell volumes. To find the temperatures and coupling parameters, it is important to first obtain the continuous macroscopic velocity function of the ions as a function of position. By symmetry, the macroscopic velocity function only has a radial component, $\bar{v}_r(r,t)$. For each of the 10 shells, $\bar{v}_r(r,t)$ is taken to be identical with a quadratic fit to the actual (microscopic) radial velocities of all ions in the shell. Since each of the shells i has its own time-dependent velocity fit parameters, we add an index i to the velocity fit functions, $\bar{v}_{r,i}(r,t)$. During the course of the up to 10 000 individual simulations, the accuracy of the fits $\bar{v}_{r,i}(r,t)$ is continually improved by taking the particle velocities of all earlier individual simulations into account when finding the fit functions $\bar{v}_{r,i}(r,t)$. The temperature of the ith shell, $T_i(t)$, is then given by the root-mean-square deviation of the particle velocities from the macroscopic average, $\bar{v}_{r,i}(r,t)\hat{r}$, with radial unit vector $\hat{r}$. While the accuracy of the fits, $\bar{v}_{r,i}(r,t)$, is critical in the described model, we note that a poor model for $\bar{v}_{r,i}(r,t)$ would result in higher temperatures and lower Coulomb coupling parameters. The results that we show are understood to be close upper bounds for the actual macroscopic temperatures $T_i(t)$ and close lower bounds for the Coulomb coupling parameters $\Gamma_i(t)$.

Once the temperatures and densities are known, in the simulation one can readily calculate other macroscopic parameters such as the Debye length, the ion acoustic velocity, and the ion-plasma frequency. Each of these parameters depends on shell index i and time.

We typically conduct 1000 to 10 000 simulations for a given set of initial macroscopic plasma conditions, and average the results for plasma density, temperature, etc. over these simulations.

B. Results of molecular dynamics model

1. Disorder-induced heating

In analogy with the experiment, in the simulation in Fig. 4 we choose (spherical) saturated Gaussians with radii of about 20 μm for the initial density profile. For the initial velocity distribution, we use a fixed velocity magnitude given by the recoil that occurs in photoionization. Photoionization of the Rb $5P_{3/2}$ state with 355 nm laser light has a kinetic-energy
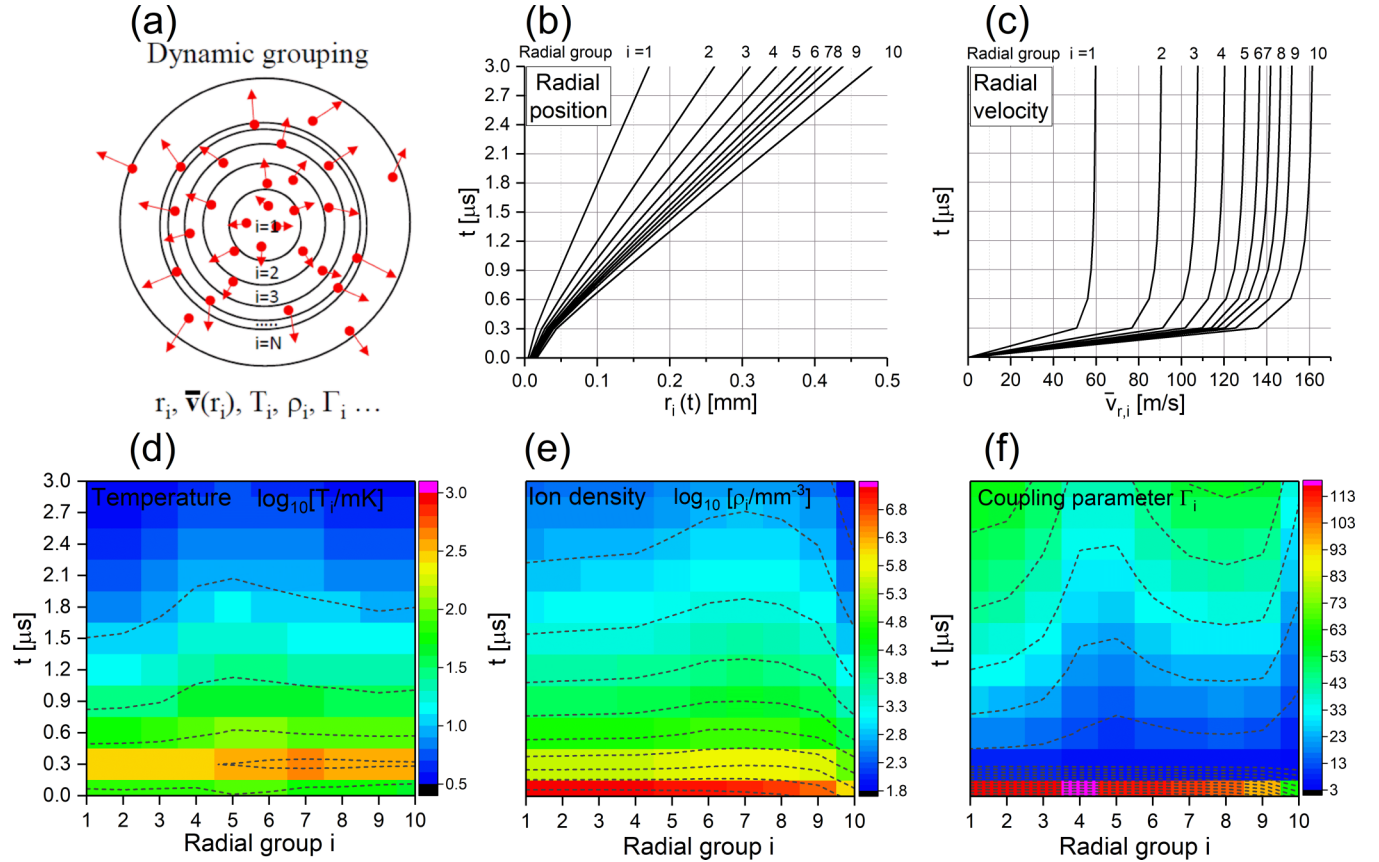
FIG. 4. (a) Sketch of the radial-partition (shell) model explained in the text. The shell radii, the macroscopic velocity $\bar{v}_{r,i}(r, t)$, and other plasma parameters depend on shell index i and time. (b) Average shell radii (horizontal axis) obtained for 125 ions with an initial cloud radius of about 20 μm vs expansion time (vertical axis). The shell indices are listed on top. (c) Corresponding average shell velocities. (d) Temperature vs shell index (horizontal axis) and time (vertical axis), displayed on a logarithmic color map. (e) Ion density vs shell index (horizontal axis) and expansion time (vertical axis), displayed on a logarithmic color map. (f) Coulomb coupling parameter Γ vs shell index (horizontal axis) and time (vertical axis), displayed on a linear color map.

release of 0.9 eV, of which 5.8 μeV is picked up by the ions. The initial distribution of ion velocity angles is given by the linear polarization direction of the photoionization laser and spherical harmonics. We choose an ion number of 125, which leads to conditions similar to our experiment. The plasma is then dense enough that the velocity distribution locally thermalizes quickly enough so that details of the photoionization are negligible (only the initial velocity magnitude has a small effect). Also, the depth of the space-charge potential well for electrons after plasma excitation is only 13 meV, i.e., in the plasmas generated by photoionizing Rb $5P_{3/2}$ atoms with 355 nm laser light, all photoelectrons (energy 0.9 eV) near-instantaneously escape from the ion plasma and do not contribute to its dynamics.

In Fig. 4, we show the density, temperature, and coupling parameter. The system is, initially, very far away from any type of equilibrium because the initial Coulomb potential energy of the disordered ion cloud, after the electrons have escaped, exceeds the photoionization recoil energy of the ions by a factor near 1000. This implies that the initial kinetic energy of the ions does not play an important role and that its initial Coulomb coupling parameter of near 100, computed from the initial density and kinetic energy, does not have

much physical meaning. We see from the temperature plot in Fig. 4 that the plasma as a whole heats up from tens of mK to near 1 K within a fraction of a microsecond; this is due to disorder-induced heating. During that time, the plasma reaches a dynamic steady state, and temperatures and coupling parameters computed for the 10 radial partitions become physically meaningful. The ion-plasma frequency $f_{p,i}$ drops from several MHz to about 0.5 MHz during that time, and the Debye length increases from sub μm to several μm. In this phase, the coupling parameter Γ traverses a low point of about six, i.e., even in this hottest phase, the plasma is strongly coupled.

2. Adiabatic expansion and shock fronts

After a few-hundred ns, the plasma transitions from heating into an adiabatic expansion phase of about one microsecond. During that phase, the particles are still collisionally coupled, while the overall acceleration caused by the Coulomb explosion fades and the spherical partitions approach a radially dependent terminal velocity. During this time, much of the initial plasma energy gets converted into the directed (nonthermal) kinetic energy of the expanding
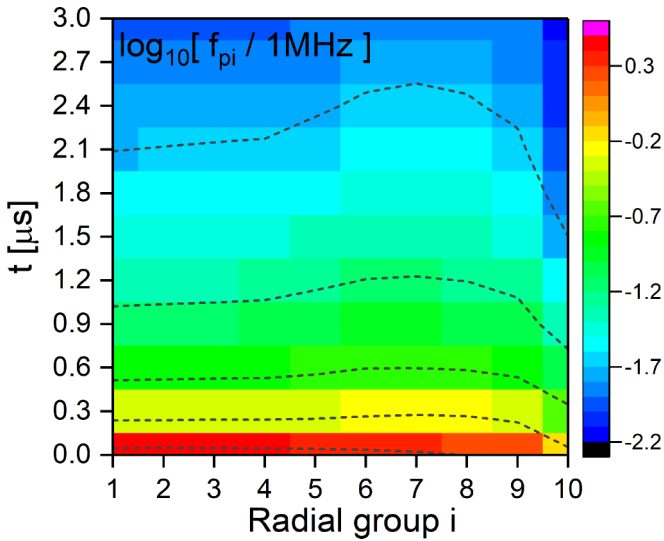
FIG. 5. Ion-plasma frequency $f_{p,i}$ from the same simulation as in Fig. 4 vs shell index (horizontal axis) and expansion time (vertical axis), displayed on a logarithmic color map.

spherical partitions. Near the end of the expansion time, in Fig. 4, the directed kinetic energy outweighs the thermal kinetic energy by a factor of about 10^4 and the potential energy vanishes. This further implies that during the adiabatic expansion, the outer spherical partitions of the plasma turn highly supersonic, reaching Mach numbers of about 40 in the outermost partitions.

In the course of adiabatic expansion, the shock front develops, as seen in a relative rise in particle density in the outer radial partitions and a radial bunching of a few radial partitions around the partition $i = 8$. Within the shock region, other macroscopic plasma parameters differ from their values in the intermediate radial region of the plasma. For instance, the temperature is about 20% lower and the coupling parameter is about 30% higher. Importantly, the coupling parameter increases, overall, and approaches $\sim$20 at about 1 μs (within the shock region). Later into the expansion, the particles collisionally mostly decouple, but the system continues to ballistically cool. After 3 μs of expansion time, the Coulomb coupling parameter exceeds 50 and the temperature has dropped to about 4 mK (from an initial photoionization recoil energy equivalent to 44 mK).

For a further discussion of collisional decoupling, in Fig. 5 we show the ion-plasma frequency vs shell index i and free-expansion time t,

$$f_{p,i}(t) = \frac{1}{2\pi} \sqrt{\frac{e^2 \, n_{V,i}(t)}{\epsilon_0 M}},$$

where M is the Rb ion mass. For our conditions, f_p can be taken to be of the order of the collision frequency because the time it takes to efficiently transfer potential into kinetic energy, and vice versa, is about one-quarter of the ion-plasma oscillation period, $1/f_{p,i}$. After its initial drop to $\sim$0.5 MHz during the first few-hundred ns, the plasma frequency $f_{p,i}$ is still sufficiently high to effectuate collisional coupling in the expanding plasma. The plasma oscillation period $1/f_{p,i}$

rapidly drops to below $0.1t$ during an expansion time $t \approx$ 1 μs. In comparison, the shock front becomes established as early as about 300 ns into the expansion. At times past $t \approx 1$ μs, the expanding plasma collisionally decouples, as the plasma frequency continues to drop to several tens of kHz near the end of the simulated expansion. As the plasma collisionally decouples, the shock front becomes frozen into the ballistically expanding system. Long-range Coulomb forces may still affect the particle-correlation function (Sec. V E) through an "annealing"-like process.

As the plasma collisionally decouples, the Coulomb coupling parameter Γ becomes ill defined because the system increasingly departs from local thermal equilibrium (due to a lack of collisions). The coupling parameters Γ in Fig. 4, at times $t \gtrsim 1$ μs, are to be interpreted as effective values that measure the ratio of potential and kinetic energy.

C. Details of fluid model

The fluid model sketched in Sec. III is well suited to qualitatively predict the formation of shock fronts. In the fluid model, the plasma is split into radial or cylindrical shells, dependent on the symmetry of the problem. A shell in the fluid model is filled with an interpenetrable fluid with fixed charge-to-mass ratio and time-dependent and shell-dependent density. The fluid shells are propagated in the time-dependent macroscopic electric field of the system following Newton's equations of motion; the electric field is computed with Gauss's law. Thermal motion, particle collisions, and microfield effects are ignored. In the fluid model, the number of shells is chosen very large, so as to arrive at an accurate description of the fluid motion (here we use up to 10 000). The shells in the fluid model are not to be confused with the partitions in the molecular dynamics model. In the former, the shell positions and velocities themselves are propagated with equations of motion involving shell masses, charges, and fields acting on the shells, whereas the latter merely serve as dynamic radial partitions within which macroscopic plasma parameters of the ion system are computed. The ion mass points follow microscopic molecular dynamics equations that have nothing to do with the partitions.

D. Results of fluid model

1. Shock front

In Fig. 6(a), the shock front forms at about 0.3 μs expansion time and becomes more prominent later (see inset). In the fluid model, the onset of the shock front occurs when initially further-inside charged shells begin to overtake initially further-outside charged shells. The radial location of the shock front is given by the condition $\Delta r_k(t)/\Delta k = 0$, where $r_k(t)$ is the radius of the kth shell at time t, and k is an integer counter that is assigned to the charged shells from the inside out, at time $t = 0$. According to this equation, the singular behavior, which is equivalent to the shock front, marks a condition where a group of shells, with indices k within a contiguous range, pile up at approximately the same radius, which is the shock-front location. This can only occur after some expansion time. At later times, the shock front becomes
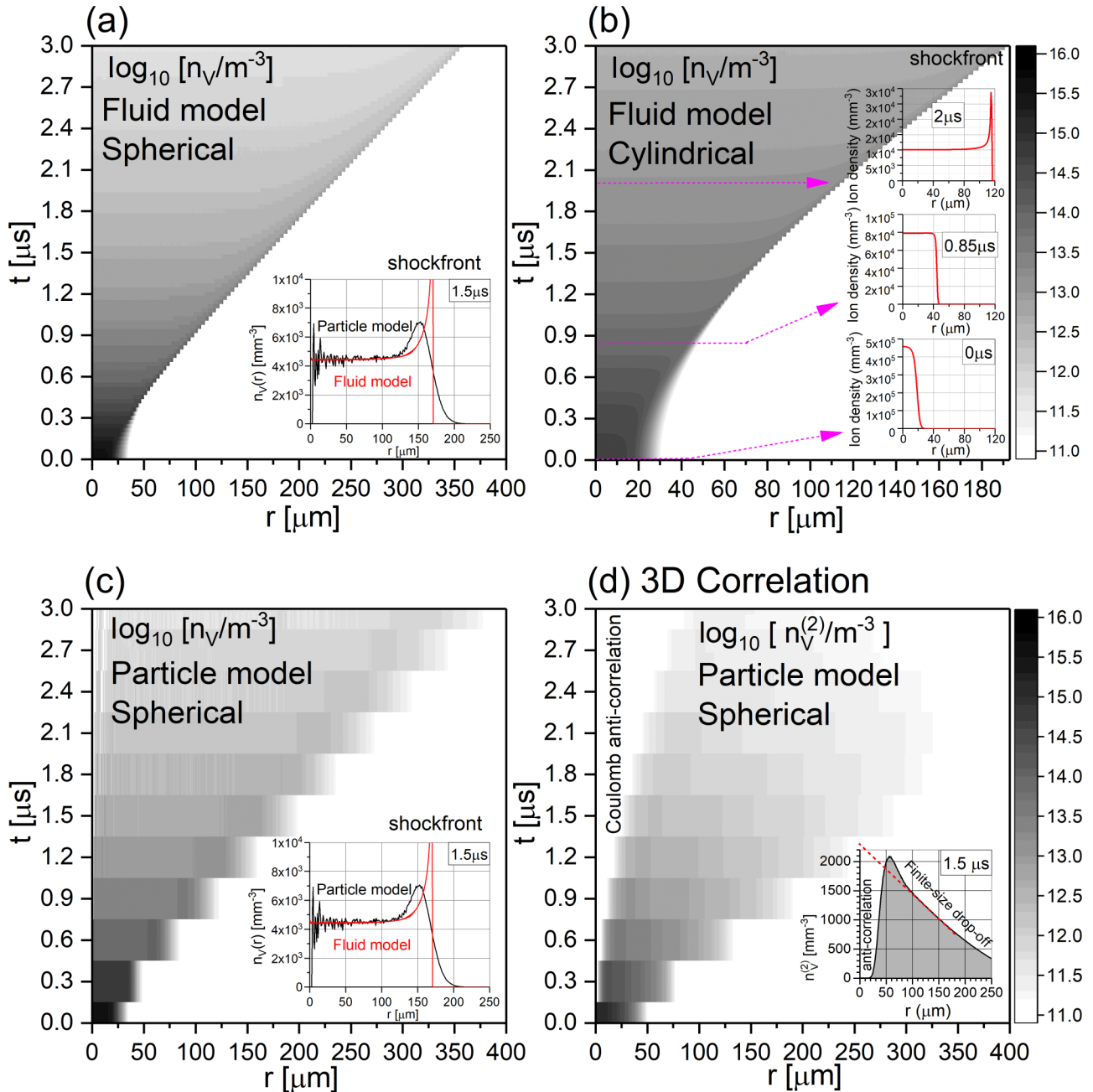
FIG. 6. Density maps vs radius r (horizontal axes) and expansion time t (vertical axes) from fluid-model simulations of the expansion of (a) a spherical and (b) an infinitely long cylindrical plasma, with radial profiles at selected times shown in the insets. (c) A molecular dynamics simulation with parameters as in (a). The insets in (a)–(c) for $t \geqslant 1.5\ \mu$s show shock-front singularities. The molecular dynamics simulation reveals that the plasma microfields broaden the shock fronts and reduce their contrast. (d) A molecular dynamics simulation of the density correlation function, $n_V^{(2)}(r, t)$, vs correlation distance r and expansion time t. The inset shows $n_V^{(2)}(r, t)$ at $t = 1.5\ \mu$s, with a trend line (red dashed line) that visualizes the overall drop due to the finite size of the plasma.

more pronounced, while in the interior region, the plasma density becomes position independent and continues to drop in time. In Fig. 6(c) and in the insets in Figs. 6(a) and 6(c), we compare the density from the fluid model with that from the particle model. It is seen that the overall behaviors are similar, as expected. However, the shock front appears as a singularity in the fluid model, whereas it manifests as a moderate density enhancement in the particle model. This is due to the fact that

the fluid model fails to account for the granularity of the mass and charge distribution and microfield effects, which act to wash out the shock front.

2. Cylindrical versus spherical plasma

In Fig. 6(b), we use the fluid model to describe the expansion of a cylindrically symmetric, infinitely long plasma with an initial radius of $\approx 20\ \mu$m, an initial saturated Gaussian

profile, and a total linear charge density of 5×10^5 e/m. These parameters correspond with those of the elongated plasma that we have studied in our experiment. It is seen in the simulations that the spherical and cylindrical systems undergo similar dynamics, as expected. The insets in Fig. 6(b) highlight the differences in the radial density profiles before, at, and well after the shock-front formation.

E. Correlations

Finally, in Fig. 6(d), we use the particle model to obtain the 3D pair-correlation function in a freely expanding, spherically symmetric plasma. Due to the small finite size of the plasma, there is no well-defined radial distance beyond which the pair-correlation function becomes stationary and equivalent with that of an uncorrelated system. Hence, a normalization akin to Fig. 3 is not possible. Instead, we plot the density correlation function $n_V^{(2)}(r)$, averaged over all particles in the plasma. (Since this quantity describes the average particle density at a three-dimensional distance r from a randomly chosen ion, it has the dimension 1 over volume.) It is seen that the density correlation function rapidly develops an anti-correlated core within which $n_V^{(2)}(r)$ drops to near identical zero. The range of this core expands to beyond 50 μm at 3 μs, and the rate of expansion keeps increasing, even after the particles collisionally decouple. This behavior accords with the finding that the Coulomb coupling continues to increase even at late times $\gtrsim 3$ μs. It may indicate that the fine-scale rearrangement of particle positions, mediated by long-range Coulomb forces, continues to affect $n_V^{(2)}(r)$ and the Coulomb coupling, even after the system becomes largely noncollisional.

A close look at Fig. 6(d) shows a significant "overshoot" immediately outside the anticorrelated core [compare $n_V^{(2)}(r)$ with the dashed line in the inset of Fig. 6(d)]. This may indicate short-range order. Similarly, the density function in Fig. 6(c) indicates a void region near $r = 0$, as well as several quasiperiodic ripples. Future modeling and experiments on 3D correlation functions and structure factors may be necessary to elucidate these observations further.

We note in this context that systems with Γ values ~ 50, as seen in Fig. 4 at times $t \gtrsim 1$ μs, would exhibit more long-range structure than the inset of Fig. 6(d) shows. For instance, Fig. 2 in [42] shows several damped oscillations in the 3D correlation function in this range of Γ. However, as discussed in Sec. V B 2, collisional decoupling at times $t \gtrsim 1$ μs requires a modification of the interpretation of Γ in terms of an effective coupling parameter; the collisional decoupling very likely prevents the system from developing long-range correlations to the same degree as those found in (near-) infinite, equilibrium systems with $\Gamma \sim 50$. The interpretation of Fig. 6(d) must further take into account the small finite size of our system. The inset in Fig. 6(d) does, indeed, only show one "overshoot" of the 3D correlation function above the trend line that indicates the finite-size-induced drop-off in our microplasma.

VI. CONCLUSION

We have observed cold-ion-plasma expansion by time-delayed ion extraction and ion imaging on a position-

resolving particle detector. Results have been compared with two models: a particle model and a fluid model. From the experimental data, we have seen that as the plasma expands, shock fronts of high ion density form at the plasma-vacuum interface (the outer layers of the expanding plasma). Our computer simulations verify that these density buildups are shock shells, which are accompanied by variations in other macroscopic plasma parameters (temperature and Coulomb coupling parameter). These results, as well as our experimental and simulated data on pair-correlation functions, show the rich dynamics of microplasma explosions into the vacuum. In future work, we plan to observe non-neutral plasmas with different initial conditions (e.g., in initial density), investigate neutral plasmas, and apply atom-based electric-field measurement techniques to diagnose the electric fields in cold plasmas [20,21]. The latter methods may enable a distinction between microscopic (Holtsmark) and macroscopic fields. To push the microscopic fields to higher values, amenable to the experimental detection of plasma electric fields, one may use the plasma focus effect shown in Fig. 2(c) to take advantage of a transient spike in plasma density. Further, in light of the high relative contrast of the 3D correlations in Fig. 6(d) in comparison with that of the 2D ones shown in Fig. 3, a measurement of the 3D correlation function can be considered.

APPENDIX: ATOMIC-PHYSICS PACKAGE AND PLASMA PREPARATION IN THE EXPERIMENT

We employ a dual-MOT vacuum chamber with a primary MOT that contains a reservoir of trapped ^{87}Rb atoms, and a secondary MOT from which the plasma is formed. Atoms are loaded from the primary MOT into the secondary with a pulsed pusher laser (1.5 mW peak power, 1 mm FWHM beam diameter, and 10 Hz repetition rate with duty cycle of 10%). The secondary MOT is able to trap clouds of several-10^7 ^{87}Rb atoms at densities of up to $\sim 4 \times 10^{11}$ cm^{-3}. The region in which the laser-generated plasma is prepared is electric-field zeroed to within 10 mV/cm using internal field compensation electrodes. The zeroing is based on observing the acceleration of small test ion samples as a function of the voltages on the compensation electrodes.

The experiment is run at a repetition rate of 10 Hz. In each cycle, a plasma is formed in the secondary MOT with a resonant two-photon photoionization process. Prior to plasma formation, the MOT light is turned off to prevent unwanted plasma outside the intended initial volume. A fraction of the cold atoms is resonantly driven by an 18-μs-long, 780 nm laser pulse to the $5P_{3/2}$ state. This laser beam has a Gaussian profile, with a waist w_0 of 9 μs, Rayleigh range of 330 μm, and central intensity of 105 I_{sat} (the saturation intensity $I_{\text{sat}} = 1.6$ mW/cm^2). Five microseconds after the 780 nm pulse is turned on, the $5P_{3/2}$ atoms are ionized with a 10 ns, 355 nm

ultraviolet pulse from a Q-switched, frequency-tripled Nd:YAG laser. This wavelength is well above the ionization threshold wavelength of 479.1 nm for atoms in the $5P_{3/2}$ state. Atoms in the intermediate state become ionized, and the liberated valence electrons have a kinetic energy of 0.9 eV, which is sufficient for the electrons to escape the plasma cloud. The initial temperature of the trapped atoms is roughly 100 μK, but the photoionization is accompanied with recoil heating to ≈ 44 mK, the initial temperature of our plasmas. While the 355 nm laser is linearly polarized, the plasmas we work with are dense enough that the laser polarization has no notable effect on ion recoil velocity distribution or initial temperature. The 355 nm pulse has a diameter of ~ 2 mm, which is much larger than the size of the 780 nm beam. Hence, the initial geometry of the plasma column is determined by the 780 nm beam size and its central intensity, and the MOT size. Further, the fluence of the 355 nm pulse is $\lesssim 10^{16}$ cm^{-2}, corresponding to a photoionization probability of the $5P_{3/2}$ atoms of $\lesssim 10$ percent, leading to up to several-hundred ions in the initial plasma volume.

[1] H. Metcalf and P. van der Straten, *Laser Cooling and Trapping* (Springer-Verlag, New York, 1999).

[2] T. C. Killian, S. Kulin, S. D. Bergeson, L. A. Orozco, C. Orzel, and S. L. Rolston, Phys. Rev. Lett. **83**, 4776 (1999).

[3] S. Kulin, T. C. Killian, S. D. Bergeson, and S. L. Rolston, Phys. Rev. Lett. **85**, 318 (2000).

[4] T. Pohl, T. Pattard, and J. M. Rost, Phys. Rev. A **68**, 010703(R) (2003).

[5] T. Pohl, T. Pattard, and J. M. Rost, Phys. Rev. Lett. **92**, 155003 (2004).

[6] N. C. Woolsey, A. D. Ash, C. Courtois, R. O. Dendy, C. D. Gregory, I. M. Hall, and J. Howe, AIP Conf. Proc. **827**, 365 (2006).

[7] P. McKenna, D. Neely, R. Bingham, and D. A. Jaroszynski, *Laser-Plasma Interactions and Applications* (Springer International, Switzerland, 2011).

[8] P. Wessels, B. Ruff, T. Kroker, A. K. Kazansky, N. M. Kabachnik, K. Sengstock, M. Drescher, and J. Simonet, Commun. Phys. **1**, 32 (2018).

[9] G. Djotyan, J. Bakos, M. Kedves, B. Ráczkevi, D. Dzsotjan, K. Varga-Umbrich, Z. Sórlei, J. Szigeti, P. Ignácz, P. Lévai, A. Czitrovszky, A. Nagy, P. Dombi, and P. Rácz, Nucl. Instr. Methods Phys. Res. A **884**, 25 (2018).

[10] P. Jiang and J. L. Roberts, Phys. Plasmas **26**, 043513 (2019).

[11] T. K. Langin, G. M. Gorman, and T. C. Killian, Science **363**, 61 (2019).

[12] M. Lyon and S. L. Rolston, Rep. Prog. Phys. **80**, 017001 (2017).

[13] M. S. Murillo, Phys. Plasmas **14**, 055702 (2007).

[14] T. Ott, M. Bonitz, L. G. Stanton, and M. S. Murillo, Phys. Plasmas **21**, 113704 (2014).

[15] N. Desbiens, P. Arnault, and J. Clérouin, Phys. Plasmas **23**, 092120 (2016).

[16] T. Sprenkle, A. Dodson, Q. McKnight, R. Spencer, S. Bergeson, A. Diaw, and M. S. Murillo, Phys. Rev. E **99**, 053206 (2019).

[17] E. Boella, B. P. Paradisi, A. D'Angola, L. O. Silva, and G. Coppa, J. Plasma Phys. **82**, 905820110 (2016).

[18] E. V. Crockett, R. C. Newell, F. Robicheaux, and D. A. Tate, Phys. Rev. A **98**, 043431 (2018).

[19] D. Feldbaum, N. V. Morrow, S. K. Dutta, and G. Raithel, Phys. Rev. Lett. **89**, 173004 (2002).

[20] D. A. Anderson, G. Raithel, M. Simons, and C. L. Holloway, arXiv:1712.08717.

[21] D. Weller, J. P. Shaffer, T. Pfau, R. Löw, and H. Kübler, Phys. Rev. A **99**, 043418 (2019).

[22] J. Sous and E. R. Grant, New J. Phys. (UK) **21**, 043033 (2019).

[23] D. Murphy, R. W. Speirs, D. V. Sheludko, C. T. Putkunz, A. J. McCulloch, B. M. Sparkes, and R. E. Scholten, Nat. Commun. **5**, 4489 (2014).

[24] J. P. Morrison and E. R. Grant, Phys. Rev. A **91**, 023423 (2015).

[25] G. T. Forest, Y. Li, E. D. Ward, A. L. Goodsell, and D. A. Tate, Phys. Rev. A **97**, 043401 (2018).

[26] U. Samir, K. H. Wright Jr., and N. H. Stone, Rev. Geophys. **21**, 1631 (1983).

[27] C. Sack and H. Schamel, Phys. Rep. **156**, 311 (1987).

[28] V. Y. Bychenkov and V. Kovalev, Plasma Phys. Rep. **31**, 178 (2005).

[29] M. Grech, R. Nuter, A. Mikaberidze, P. Di Cintio, L. Gremillet, E. Lefebvre, U. Saalmann, J. M. Rost, and S. Skupin, Phys. Rev. E **84**, 056404 (2011).

[30] R. W. Gould, Phys. Plasmas **2**, 2151 (1995).

[31] D. Walsh and D. H. E. Dubin, Phys. Plasmas **25**, 052119 (2018).

[32] A. E. Kaplan, B. Y. Dubetsky, and P. L. Shkolnikov, Phys. Rev. Lett. **91**, 143401 (2003).

[33] R. P. Drake, *High-Energy-Density Physics: Foundation of Inertial Fusion and Experimental Astrophysics* (Springer International, Berlin, 2006).

[34] B. S. Zerbe, X. Xiang, C.-Y. Ruan, S. M. Lund, and P. M. Duxbury, Phys. Rev. Accel. Beams **21**, 064201 (2018).

[35] T. Pohl, T. Pattard, and J. M. Rost, Phys. Rev. Lett. **94**, 205003 (2005).

[36] A. Schwarzkopf, D. A. Anderson, N. Thaicharoen, and G. Raithel, Phys. Rev. A **88**, 061406(R) (2013).

[37] N. Thaicharoen, A. Schwarzkopf, and G. Raithel, Phys. Rev. A **92**, 040701(R) (2015).

[38] J. Grimmel, M. Stecker, M. Kaiser, F. Karlewski, L. Torralbo-Campo, A. Günther, and J. Fortágh, Phys. Rev. A **96**, 013427 (2017).

[39] M. Stecker, R. Nold, L.-M. Steinert, J. Grimmel, D. Petrosyan, J. Fortágh, and A. Günther, arXiv:1905.08221.

[40] K. Gawlas and S. D. Hogan, Phys. Rev. A **99**, 013421 (2019).

[41] Y. C. Chen, C. E. Simien, S. Laha, P. Gupta, Y. N. Martinez, P. G. Mickelson, S. B. Nagel, and T. C. Killian, Phys. Rev. Lett. **93**, 265003 (2004).

[42] Z. Donkó, J. Phys. A: Math. Theor. **42**, 214029 (2009).